Picosecond phase-velocity dispersion of hypersonic phonons imaged with ultrafast electron microscopy

Daniel R. Cremons,[*] Daniel X. Du, and David J. Flannigan[†]

Department of Chemical Engineering and Materials Science, University of Minnesota, 421 Washington Ave. SE,
Minneapolis, Minnesota 55455, USA

Here, we describe the direct imaging—with four-dimensional ultrafast electron microscopy—of the emergence, evolution, dispersion, and decay of photoexcited, hypersonic coherent acoustic phonons in nanoscale germanium wedges. Coherent strain waves generated via ultrafast *in situ* photoexcitation were imaged propagating with initial phase velocities of up to 35 km/s across discrete micrometer-scale crystal regions. We observe that, while each wave front travels at a constant velocity, the entire wave train evolves with a time-varying phase-velocity dispersion, displaying a single-exponential decay to the longitudinal speed of sound (5 km/s) and with a mean lifetime of 280 ps. We also find that the wave trains propagate along a single in-plane direction oriented parallel to striations introduced during specimen preparation, independent of crystallographic direction. Elastic-plate modeling indicates the dynamics arise from excitation of a single, symmetric (dilatational) guided acoustic mode. Further, by precisely determining the experiment time-zero position with a plasma-lensing method, we find that wave-front emergence occurs approximately 100 ps after femtosecond photoexcitation, which matches well with Auger recombination times in germanium. We conclude by discussing the similarities between the imaged hypersonic strain-wave dynamics and electron/hole plasma-wave dynamics in strongly photoexcited semiconductors.

I. INTRODUCTION

Intense, ultrafast photoexcitation of charge carriers in semiconducting materials produces a highly nonequilibrium condition that evolves via a wealth of relatively complex, interwoven energy-cascade processes, including electron-electron and electron-atom scattering, optical- and acoustic-phonon excitation, strain-wave launch and propagation, and thermal diffuse heating [1,2]. These interdependent and spatially varying effects occur across spatiotemporal scales that span many orders of magnitude, and the initial transient behaviors are sensitively dependent upon the nature of photoexcitation [3]. While discrete emergent behaviors may be experimentally deconvoluted and individually quantified in the time domain, interaction of photoexcited (quasi)particles (electrons and holes, excitons, phonons) with ever-present atomic and nanoscale defects and strain fields, and especially within confined geometries, can result in the rapid and hard-to-predict evolution of dynamics. In addition, the random and heterogeneous nature of impurity and defect distributions within the crystal lattice further adds to the complexity, thus necessitating the study of dynamics on requisite scales in order to develop detailed and comprehensive descriptions. As such, development and application of ultrafast experimental methods capable of directly probing structural dynamics (e.g., femtosecond x-ray and electron scattering) has resulted in an increased level of understanding of photoinduced effects in otherwise well-characterized, archetypal semiconducting materials [4–9].

One of several energy conversion and relaxation processes arising from optical excitation of semiconductors is the generation of coherent, gigahertz (GHz) acoustic-phonon wave trains arising from a combination of deformation potential and thermoelasticity (i.e., a redistribution of charge-carrier population leading to a change in bond strengths and a transient lattice thermal expansion, respectively) [10,11]. The precise mechanistic details are dependent upon scattering and recombination rates that are dictated by both structural and electronic properties. Accordingly, prediction and control of energy evolution and conversion is predicated upon deconvoluting and ultimately tuning the dominant electron-lattice coupling mechanisms. Further, once generated, coherent strain waves can undergo several spatiotemporally dependent behaviors (e.g., mode conversion, diffraction, and coupling to topographic features) that will modify the specific energy-relaxation pathways and timelines in nanoscale and nanostructured systems [12–14]. Because the propagating strain waves produce a localized, ultrafast elastic lattice deformation, certain aspects are well-suited for study with femtosecond (fs) diffraction methods, wherein particular phonon behaviors are determined from spatially averaged momentum and intensity changes in coherently-scattered x-ray photons or electrons [15–25]. Despite intense and sustained examination, however, there is still much to be learned about the spatiotemporal evolution of several fundamental acoustic strain-wave behaviors—including coupling dynamics, time-varying phase velocities, preferred propagation directions, and time-domain dispersions.

Here we report physical insight into the fundamental behavior of photoexcited acoustic phonons obtained via direct-imaging methods with fs transmission electron microscopy [26–31]. With combined picosecond-nanometer real-space resolutions, we directly imaged the optical excitation of

---

[*]Present address: NASA Goddard Space Flight Center, 8800 Greenbelt Rd., Greenbelt, Maryland 20771, USA.

[†]Corresponding author: flan0076@umn.edu

GHz coherent strain waves that propagate with initial hypersonic phase velocities (measurable up to 35 km/s) in thin, freestanding, single-crystal germanium (Ge) wedges. By imaging transient behaviors of individual, nanoscale phonon wave fronts, we discovered a time-dependent phase-velocity dispersion; while the velocity of each individual wave front is constant, the entire wave train displays a single-exponential decay in phase velocity to the longitudinal speed of sound (5 km/s), with a mean lifetime of 280 ps. We also directly imaged the evolution of individual phonon wave-front shapes and lengths, and we observed that the wave trains propagate along single in-plane directions oriented parallel to striations in the crystal arising from mechanical polishing, rather than along a preferred crystallographic direction. Further, for the experimental conditions used here, we spatially resolved the formation of the first phonon wave fronts, which occurs approximately 100 ps after fs photoexcitation, suggestive of strain-wave generation from Auger recombination and subsequent lattice heating [16,32,33]. Calculations using a linear-elastic plate model indicate that excitation of a single, symmetric (dilatational) guided acoustic mode, which is nondispersive in the frequency domain, is responsible for the imaged structural dynamics.

II. METHODS

The experimental setup was similar to what has previously been used to directly image acoustic-phonon dynamics [34–37]. The general configuration is as follows. A 200-kV transmission electron microscope (TEM) equipped with a thermionic electron gun and lanthanum hexaboride (LaB$_6$) source is modified to have vacuum-compatible optical ports at the gun and specimen regions. Pump-probe experiments are conducted by interfacing this TEM with a diode-pumped, solid-state fs laser with a 1.03-μm fundamental wavelength (λ) output. Pulses from this laser are split to form separate pump and probe beamlines. Specifically here, pulses comprising the pump line were either left as is (i.e., $\lambda = 1.03\,\mu$m; $h\nu = 1.2$ eV, where h is the Planck constant and ν is the light frequency) or were frequency doubled to $\lambda = 515$ nm ($h\nu = 2.4$ eV) and were used to excite an approximately 100-μm diameter spot (full width at half maximum, FWHM) on undoped Ge specimens *in situ*. Pulses in the probe line were frequency quadrupled to $\lambda = 257$ nm and were trained on the LaB$_6$ source to generate discrete photoelectron packets. Laser-pulse durations were stretched from 220 to 700 fs FWHM, resulting in an instrument-response time of 1 to 2 ps FWHM for packets containing between 200 and 800 photoelectrons, respectively [38]. The relative arrival times of the pump pulses and probe packets at the specimen were controlled with a 1-m optical delay stage, and the moment of optical excitation (i.e., time zero) was determined with a so-called plasma-lensing method [38–40]. Additional experimental details for specimen preparation, the TEM, and the laser system can be found in Supplemental Material [41].

III. RESULTS AND DISCUSSION

In general, direct imaging with an ultrafast electron microscope (UEM) of photoexcited, propagating acoustic-phonon wave fronts in crystalline materials is accomplished by monitoring transient localized changes in lattice orientation with respect to a fixed incident probe-photoelectron wave vector ($\bar{k}_I$) [37]. Here, the thin (50 to 90 nm) crystalline Ge specimens have a reciprocal lattice consisting of positions approximated by rods rather than points, with the Bragg-scattering intensity distribution within the length of the rods represented by a Bessel function. As the coherent strain waves propagate across a specimen region oriented near an allowed Bragg-scattering condition (i.e., where the angle between $\bar{k}_I$ and the atomic planes is near the Bragg angle), the reciprocal lattice is made to locally oscillate about the fixed Ewald sphere [20,25,37]. This produces a commensurate localized oscillating scattering condition that results in coherent, traveling contrast-strength modulation in real space (i.e., contrast waves) [34]. Accordingly, for UEM bright-field (dark-field) imaging, the coherent propagating strain waves can be visualized as dark (light) traveling contrast bands by blocking diffracted (direct) photoelectrons with a postspecimen objective aperture and selecting the image plane of the objective lens to be the object of the first projection-system lens (Fig. 1). In this way, the spatiotemporal evolution of coherent, photoexcited acoustic-phonon dynamics can be elucidated by quantifying UEM image-contrast dynamics.

Figure 2 summarizes the UEM imaging of hypersonic acoustic-phonon wave fronts in Ge. Following fs photoexcitation, the resulting coherent strain waves propagate along a single in-plane direction, with measured initial phase velocities that greatly exceed the longitudinal speed of sound (e.g., 35 km/s compared to 5 km/s). This was determined by tracking and quantifying each individual phonon wave front that produced a measurable contrast-strength modulation within the region of interest. As described in Supplemental Material [41], care was taken to objectively identify wave-train propagation vectors and to avoid obfuscation of intrinsic phase velocities by potential temporal aliasing effects. In this way, and by conducting imaging (and control) experiments on multiple specimens and across several regions of interest, the robustness and the reproducibility of the observed phenomena were confirmed.

In addition to initial hypersonic phase velocities, the wave-train propagation vectors are oriented along linear, nanoscale striations caused by debris generated during mechanical thinning of the bulk Ge crystal. These defects appear as linear, stationary contrast features in bright-field TEM images and UEM videos (see Fig. S10 and UEM Videos S1 and S2 in Supplemental Material [41]). Importantly, the propagation vectors observed across multiple specimens do not correspond to any single (i.e., preferred) crystallographic direction, as determined using correlative imaging and diffraction [42]. For example, for the specimen featured in UEM Video S1, the wave-front propagation direction is nearest to the [$\bar{2}$24] direction, while for UEM Video S2 (different specimen), the direction is nearest to the [$\bar{1}$13] direction. Further, while the wave trains generally emerge from the vacuum/crystal interface, the local boundary conditions of the wedge specimen do not appear to strongly influence the nanometer-scale wave-front shapes or the precise propagation directions; it can be seen in Fig. 2 and Video S1 that the wedge edge
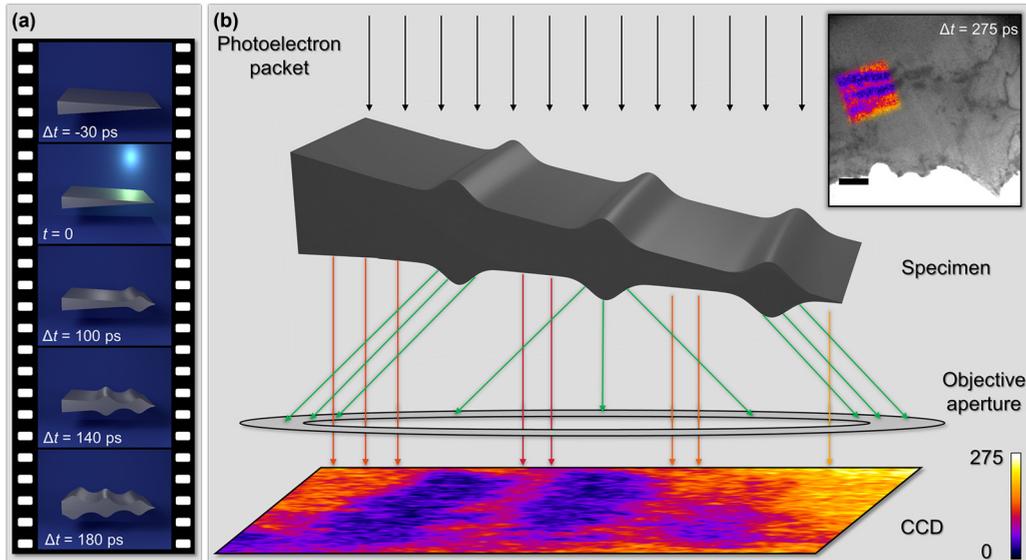
FIG. 1. Origin of time-varying UEM image contrast arising from acoustic-phonon wave trains. (a) Illustration of wave-train formation resulting from fs *in situ* photoexcitation of a freestanding wedge at $t = 0$. The time with respect to photoexcitation (Δt) is labeled in each frame. Note that the photoexcitation spot size, shown here as illuminating only a portion of the specimen for illustrative purposes, is 100-μm FWHM—many times larger than the field of view. (b) Contrast pattern in UEM bright-field imaging arising from a coherent phonon wave train. All critical components are labeled. The direct photoelectrons (hotter-colored arrows) are selected with an objective aperture to form the image. In dark-field imaging, a particular diffracted beam (green arrows) is selected to form the image (see Supplemental Material for UEM dark-field imaging experiments [41]). The inset shows a representative UEM bright-field image of the edge of a freestanding Ge wedge obtained 275 ps after photoexcitation ($\Delta t = 275$ ps). The false-colored region of interest is the same as that projected onto the charge-coupled device (CCD) in the schematic, and the corresponding color bar represents the raw-image counts. The scale bar in the inset represents 1 μm.

(formed via fracturing during the latter stages of mechanical polishing) is oriented, on average, approximately 20° off perpendicular to the direction of the striations. It is known that the shear forces used during mechanical polishing can introduce residual strains, thus altering the lattice and the electronic properties [43–45]. We therefore hypothesize that a residual strain introduced during polishing of the Ge crystal acts as a guide for the acoustic-phonon wave fronts; this will be the subject of a future study.

While the phase velocity of individual wave fronts is constant during propagation, a time-varying phase-velocity dispersion of the entire wave train occurs over approximately 1 ns following photoexcitation (see UEM Videos S1 and S2 in Supplemental Material [41]). That is, each subsequent wave front propagates with a reduced phase velocity relative to its predecessor. This effect can be graphically visualized by reducing the spatial dimensionality of the UEM images and plotting one-dimensional image intensity as a function of time [Fig. 3(a)]. In this way, the individual phonon wave fronts in the 30-GHz wave train appear as dark lines spanning specific crystal regions, with the phase-velocity dispersion manifesting as a gradual decrease in the slope of subsequent lines with increasing Δt. From this, the velocity of each wave front is readily determined, and the functional form of the time-varying phase-velocity dispersion can be deduced [Fig. 3(b)]. Notably, the single-exponential decay of the phase-velocity dispersion, from initially hypersonic values, asymptotes to the range of ultrasonically measured sound speeds in bulk Ge at 300 K (4.97 to 5.62 km/s, depending upon crystallographic direction) [46]. Further, the mean phonon-dispersion lifetime is 280 ± 10 ps

(error derived from the fit), suggesting the energy-cascade effects leading to population of the observed acoustic-phonon branch following photoexcitation are relatively long-lived. Note that the estimated photothermal temperature rise in the Ge specimen will produce a slightly *reduced* speed of sound that would increase to the values at 300 K during cooling (see Supplemental Material for calculations of the temperature-dependent bulk speed of sound in Ge [41]). Thus, the effects of diffuse lattice heating via laser excitation are unlikely to be the source of the observed dispersion behavior.

In addition to subnanosecond velocity-dispersion and phonon-relaxation times, it can be seen in Fig. 3 that a significant temporal lag occurs between time zero and emergence of the first phonon wave front, with the first observable contrast-generating dynamics appearing 60 to 80 ps after the precise moment of photoexcitation. That is, while coherent contrast waves strong enough for rigorous velocity measurements appear roughly 200 ps after photoexcitation, dynamics producing weaker transient features emerge at earlier times, although still well after time zero [e.g., faint, near-vertical lines first appear near $\Delta t = 100$ ps in Fig. 3(a)]. Importantly, myriad non-contrast-causing structural and electronic processes occur during the first 100 ps after fs photoexcitation. For example, intraband relaxation to band edges occurs following above-gap photoexcitation, which leads to the population of optical-phonon branches [47]. In the case of the generation of a dense, nonequilibrium charge-carrier plasma, such electron-lattice coupling processes decay over tens to hundreds of picoseconds via a hot-phonon bottleneck effect [48,49]. Thus, the relatively extended lifetime of intraband relaxation following above-gap
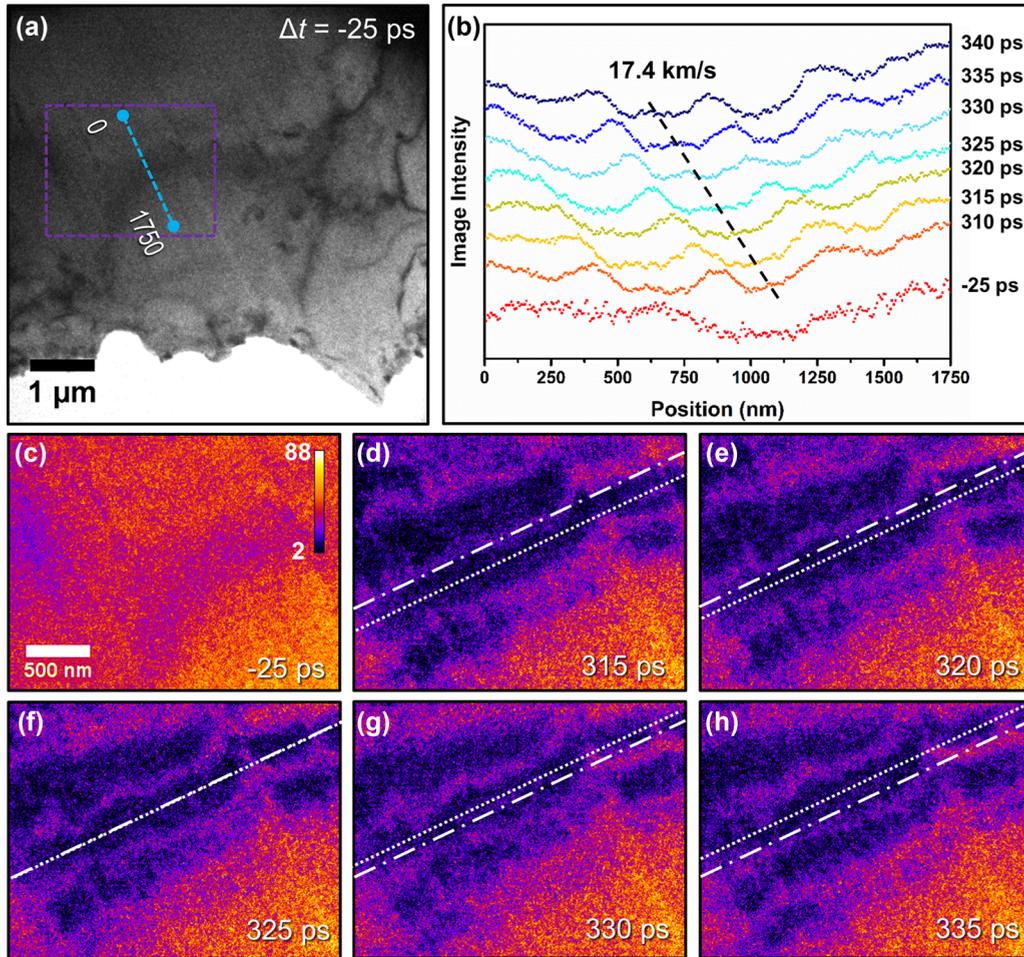
FIG. 2. Bright-field UEM imaging of directional, hypersonic acoustic phonons. (a) Representative UEM image of a Ge specimen region of interest acquired 25 ps prior to photoexcitation (i.e., $\Delta t = -25$ ps). The dashed blue line spanning from 0 to 1.75 μm (labeled in nanometers in the panel) marks the area from which time-varying image line scans, shown in panel (b), were generated, while the dashed purple rectangle denotes the region from which select, false-colored frames were extracted [panels (c) through (h)]. The dashed blue line is oriented parallel to the wave-train propagation direction and to the striation defects. (b) Line scans from select images illustrating the traveling nature of coherent contrast waves passing through the specimen region of interest. The dashed black line labeled 17.4 km/s tracks the center of an individual wave front (dark feature in the bright-field image series) within a time window spanning 310 to 340 ps after photoexcitation. A line scan from a pre-time-zero image ($\Delta t = -25$ ps) is included for comparison. The data are offset for clarity. (c) The $\Delta t = -25$-ps region of interest (false colored) from the area highlighted in (a). The color bar is scaled to the raw-image counts. (d)–(h) Select frames spanning 315 to 335 ps after photoexcitation highlighting the single traveling wave front quantified in (b). The dashed-dotted white line marks the position of the wave-front leading edge at $\Delta t = 315$ ps (i.e., this line is in the same spatial position in all frames), while the dotted white line tracks the center of the same wave front over time (i.e., this line moves with the traveling wave front).

photoexcitation, and the subsequent long-lived carrier recombination in Ge (primarily through Auger recombination) [32], is strongly correlated with the observed delay in emergence of the spatially resolved velocity-dispersive acoustic modes and the imaged strain-wave behaviors [4,16].

To better understand the imaged strain-wave behaviors and the charge-carrier/lattice coupling mechanisms, fixed-fluence, above-gap photoexcitation experiments with different photon energies were conducted on the same wedge specimen (Fig. 4 and UEM Video S2 in Supplemental Material [41]). Here, based on the incident laser fluence (1.8 mJ/cm^2) and by using the optical properties of bulk, single-crystal Ge (band gap = 0.67 eV), charge-carrier densities of 1.8×10^{20} and 3.7×10^{21} cm^{-3} were generated for incident photon energies of $h\nu = 1.2$ and 2.4 eV, respectively. Despite a factor of 20

difference in density, the quantitative behaviors of the phase-velocity dispersion and the temporal lag were unchanged. That is, the same dispersion dynamics were observed, with similar temporal onsets, phase velocities, decay times, and asymptotic behaviors [Fig. 4(a)]. This, however, was not the case for the observed contrast strength generated by the phonon wave trains, which was found to be strongly dependent on charge-carrier density, with a roughly 50% increase in amplitude for 2.4-eV photons despite similar (nondispersive) 30-GHz temporal frequencies (see Supplemental Material, especially Video S2 [41]) [Fig. 4(b)]. This suggests that wave fronts generated from relaxation of denser charge-carrier plasmas are associated with larger elastic lattice strains.

In order to determine the nature of the spatially resolved coherent strain waves and the origin of the hypersonic
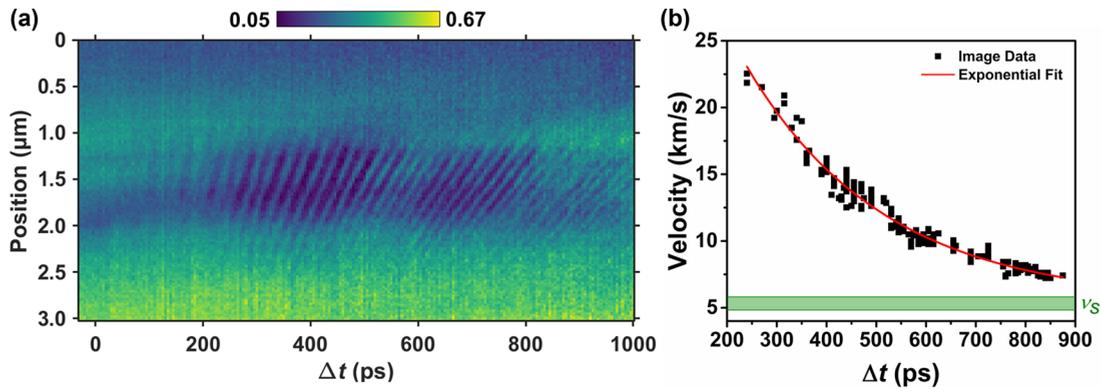
FIG. 3. Time-dependent phase-velocity dispersion of hypersonic acoustic phonons. (a) Position-time plot of coherent phonon wave fronts passing through the specimen region of interest highlighted in Fig. 2. The dark, linear features between 1.0 and 2.0 μm and beginning at approximately $\Delta t = 200$ ps arise from individual traveling wave fronts. Note that time zero ($\Delta t = 0$ ps) corresponds to the precise moment of fs photoexcitation, as determined with a plasma-lensing method (see Supplemental Material for experimental details of this method [41]). The free edge of the Ge wedge is toward larger position values; the wave-front propagation direction is from larger to smaller positions (i.e., the wave fronts emerge near the vacuum/crystal interface). The color bar represents the fractional specimen image intensity relative to the average intensity of the vacuum region at each Δt. (b) Time-varying phase-velocity dispersion, as determined from each individual wave front in (a). A single exponential fit of the extracted phase velocities is shown in red. The green band represents the range of values for the longitudinal speed of sound in Ge at 300 K.

phase-velocity dispersion, comparisons to documented behaviors of dense, photoexcited electron-hole plasmas and guided (Lamb) acoustic modes were made. Importantly, the charge-carrier/lattice coupling mechanisms associated with thermoelasticity and deformation potential evolve on significantly different timescales. While thermoelasticity occurs via excitation of incoherent phonons through subpicosecond, intraband relaxation of charge carriers, the deformation potential is instead a function of interband relaxation (picoseconds to nanoseconds) over the lifetime of the electron-hole plasma [10,11]. Accordingly, the delays in emergence, the extended lifetimes, and the coherent nature of the wave trains observed here suggest the dominant coupling process involves the deformation potential. Interestingly, intense above-gap

photoexcitation of undoped Ge produces a dense electron-hole plasma wave that propagates outward at hypersonic velocities [19,50,51], and it has been predicted that this plasma wave slows to the material sound velocity based on the ambipolar diffusion rate [11]. Further, it has been suggested that acoustic-type oscillations of the plasma waves will develop in semiconductors having large differences in electron and hole effective masses (e.g., Ge and GaAs), and that these traveling waves will display a time-dependent phase-velocity dispersion, as observed here for the coherent lattice strain waves [52].

While the similarities between hypersonic electron-hole plasma waves and the spatially resolved phonon wave trains—in addition to the strong dependence of strain-wave amplitude
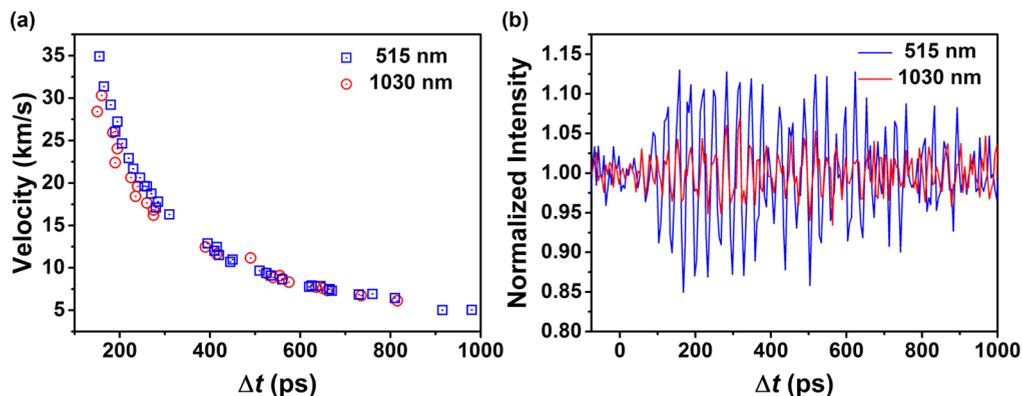
FIG. 4. Time-varying phase-velocity dispersion, strain-wave amplitude, and temporal lag for 515-nm and 1.03-μm photoexcitation. (a) Time-varying phase-velocity dispersion for excitation at $\lambda = 515$ nm ($h\nu = 2.4$ eV, blue squares) and 1.03 μm (1.2 eV, red circles). Note that time zero ($\Delta t = 0$ ps) was precisely determined using a plasma-lensing method (see Supplemental Material for details of this method [41]). (b) Intensity response from a 20 × 20-pixel image region as a function of time for 515-nm (blue) and 1.03-μm (red) excitation. The values are normalized to the pre-time-zero intensity. It can be seen that the time traces are in phase and have the same frequency, although the oscillation amplitudes are larger for the higher-energy photoexcitation (see Supplemental Material for a fast Fourier transform of the time-domain oscillations [41]).
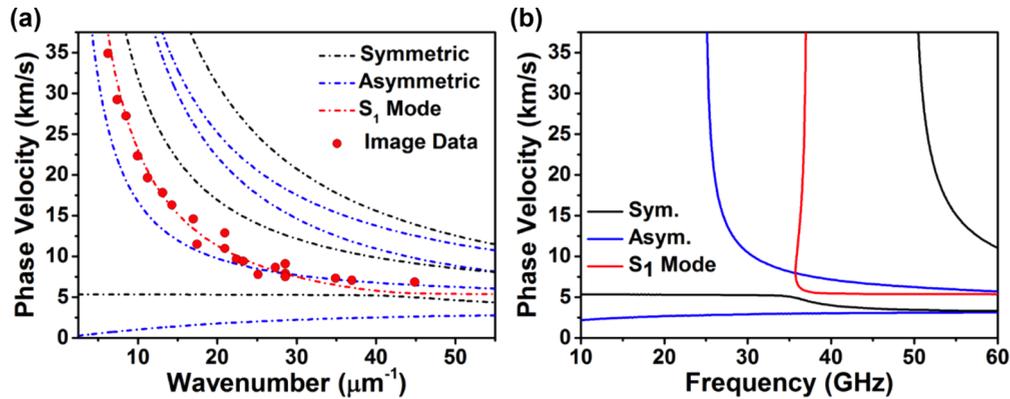
FIG. 5. Imaged phase-velocity dispersion compared to calculated guided acoustic modes. (a) Experimental wave-front phase velocity as a function of wave number (red dots) compared to symmetric and asymmetric dispersion relations (black and blue dotted-dashed curves, respectively) calculated using a linear-elastic plate model with Ge bulk material constants. The calculated first-order symmetric mode (S_1) well-matched by the image data is highlighted as a red dotted-dashed curve. (b) Calculated phase-velocity dispersion as a function of frequency for the first few symmetric and asymmetric modes (black and blue, respectively). The essentially nondispersive S_1 mode, which is well-matched by the experimentally observed behavior, is highlighted in red.

on charge-carrier density—suggest a possible charge-carrier/lattice coupling mechanism, the physical nature of the strain waves themselves is comparable to Lamb-type acoustic modes in thin, nanoscale membranes [53–55]. This is especially apparent when plotting the phase velocity of each phonon wave front as a function of corresponding measured wave number and comparing the results to the calculated dispersion relation for a Ge plate (see Supplemental Material for modeling details [41]) [Fig. 5(a)]. Because each wave front exhibits a distinct phase velocity and wave number, the generation of each wave is a separate, non-steady-state relaxation event. Here, the wave-number dispersion measured via UEM imaging closely matches that of the first-order symmetric Lamb mode (S_1). In addition, the measured temporal frequencies are well-matched by this mode [Fig. 5(b)]; the model calculations return a 36-GHz temporal frequency for the S_1 mode, which is essentially nondispersive over the experimentally measured phase-velocity range, as observed here. Note that, while the experimental wave-number dispersion is also near the first-order asymmetric (A_1) mode, which is expected to have a larger out-of-plane displacement, an increase in frequency over the measured phase-velocity range would also be expected. Also note that, while the positions of the dispersion curves are dependent on specimen thickness, the shapes are not (see Supplemental Material for the model equations [41]). This, together with the observed constant phase velocity for each individual wave front and the excellent agreement with the uniform elastic-plate model, indicates the thickness variation across the region of interest does not dictate the observed dynamics.

IV. CONCLUSIONS

In conclusion, physical insight into the fundamental nature of photogenerated coherent strain-wave dynamics in an archetypal semiconductor has been revealed via picosecond-nanometer real-space imaging with four-dimensional ultrafast electron microscopy. Specifically, the ability to image dynam-

ics on the requisite spatiotemporal scales has enabled the direct visualization of acoustic-phonon wave fronts propagating at hypersonic phase velocities, the observation of a time-varying phase-velocity dispersion to bulk sound speeds, and the spatiotemporal resolution of structural dynamics bearing striking similarities to charge-carrier plasma-wave dynamics. In addition to insight into nanoscale coherent structural dynamics, this work illustrates, in general, the usefulness of training emerging measurement techniques on seemingly well-understood materials. The result here is an increase in the understanding of fundamental strain-wave behaviors in photoexcited semiconductors and the resulting energy-cascade effects, especially with respect to the precise nature and spatial distribution of charge-carrier/lattice coupling processes and commensurate coherent behaviors (e.g., delays in wave-front formation matching Auger recombination times and single wave-front propagation directions). Looking forward, the results and methods reported here could inform a wide array of current phononic design and control applications, from energy-harvesting and diagnostics, to nascent emerging technologies such as acoustic cloaking [56–60].

[1] A. Othonos, J. Appl. Phys. **83**, 1789 (1998).

[2] J. Shah, *Ultrafast Spectroscopy of Semiconductors and Semiconductor Nanostructures* (Springer, New York, 1999).

[3] S. K. Sundaram and E. Mazur, Nat. Mater. **1**, 217 (2002).

[4] A. H. Chin, R. W. Schoenlein, T. E. Glover, P. Balling, W. P. Leemans, and C. V. Shank, Phys. Rev. Lett. **83**, 336 (1999).

[5] C. W. Siders, A. Cavalleri, K. Sokolowski-Tinten, C. Tóth, T. Guo, M. Kammler, M. H. v. Hoegen, K. R. Wilson, D. v. d. Linde, and C. P. J. Barty, Science **286**, 1340 (1999).

[6] A. Rousse, C. Rischel, S. Fourmaux, I. Uschmann, S. Sebban, G. Grillon, P. Balcou, E. Foster, J. P. Geindre, P. Audebert, J. C. Gauthier, and D. Hulin, Nature (London) **410**, 65 (2001).

[7] M. Harb, R. Ernstorfer, C. T. Hebeisen, G. Sciaini, W. Peng, T. Dartigalongue, M. A. Eriksson, M. G. Lagally, S. G. Kruglik, and R. J. Dwayne Miller, Phys. Rev. Lett. **100**, 155504 (2008).

[8] A. Yurtsever and A. H. Zewail, Science **326**, 708 (2009).

[9] M. Trigo, M. Fuchs, J. Chen, M. P. Jiang, M. Cammarata, S. Fahy, D. M. Fritz, K. Gaffney, S. Ghimire, A. Higginbotham, S. L. Johnson, M. E. Kozina, J. Larsson, H. Lemke, A. M. Lindenberg, G. Ndabashimiye, F. Quirin, K. Sokolowski-Tinten, C. Uher, G. Wang, J. S. Wark, D. Zhu, and D. A. Reis, Nat. Phys. **9**, 790 (2013).

[10] C. Thomsen, H. T. Grahn, H. J. Maris, and J. Tauc, Phys. Rev. B **34**, 4129 (1986).

[11] P. Ruello and V. E. Gusev, Ultrasonics **56**, 21 (2015).

[12] T. Pezeril, P. Ruello, S. Gougeon, N. Chigarev, D. Mounier, J. M. Breteau, P. Picart, and V. Gusev, Phys. Rev. B **75**, 174307 (2007).

[13] J. Cuffe, O. Ristow, E. Chávez, A. Shchepetov, P.-O. Chapuis, F. Alzina, M. Hettich, M. Prunnila, J. Ahopelto, T. Dekorsy, and C. M. Sotomayor Torres, Phys. Rev. Lett. **110**, 095503 (2013).

[14] A. A. Maznev, F. Hofmann, J. Cuffe, J. K. Eliason, and K. A. Nelson, Ultrasonics **56**, 116 (2015).

[15] C. Rose-Petruck, R. Jimenez, T. Guo, A. Cavalleri, C. W. Siders, F. Raksi, J. A. Squier, B. C. Walker, K. R. Wilson, and C. P. J. Barty, Nature (London) **398**, 310 (1999).

[16] A. Cavalleri, C. W. Siders, F. L. H. Brown, D. M. Leitner, C. Tóth, J. A. Squier, C. P. J. Barty, K. R. Wilson, K. Sokolowski-Tinten, M. Horn von Hoegen, D. von der Linde, and M. Kammler, Phys. Rev. Lett. **85**, 586 (2000).

[17] A. M. Lindenberg, I. Kang, S. L. Johnson, T. Missalla, P. A. Heimann, Z. Chang, J. Larsson, P. H. Bucksbaum, H. C. Kapteyn, H. A. Padmore, R. W. Lee, J. S. Wark, and R. W. Falcone, Phys. Rev. Lett. **84**, 111 (2000).

[18] D. A. Reis, M. F. DeCamp, P. H. Bucksbaum, R. Clarke, E. Dufresne, M. Hertlein, R. Merlin, R. Falcone, H. Kapteyn, M. M. Murnane, J. Larsson, T. Missalla, and J. S. Wark, Phys. Rev. Lett. **86**, 3072 (2001).

[19] M. F. DeCamp, D. A. Reis, A. Cavalieri, P. H. Bucksbaum, R. Clarke, R. Merlin, E. M. Dufresne, D. A. Arms, A. M. Lindenberg, A. G. MacPhee, Z. Chang, B. Lings, J. S. Wark, and S. Fahy, Phys. Rev. Lett. **91**, 165502 (2003).

[20] M. Harb, W. Peng, G. Sciaini, C. T. Hebeisen, R. Ernstorfer, M. A. Eriksson, M. G. Lagally, S. G. Kruglik, and R. J. Dwayne Miller, Phys. Rev. B **79**, 094301 (2009).

[21] A. Yurtsever and A. H. Zewail, Proc. Natl. Acad. Sci. USA **108**, 3152 (2011).

[22] A. Yurtsever, S. Schaefer, and A. H. Zewail, Nano Lett. **12**, 3772 (2012).

[23] W. X. Liang, G. M. Vanacore, and A. H. Zewail, Proc. Natl. Acad. Sci. USA **111**, 5491 (2014).

[24] J. B. Hu, G. M. Vanacore, A. Cepellotti, N. Marzari, and A. H. Zewail, Proc. Natl. Acad. Sci. USA **113**, E6555 (2016).

[25] L. L. Wei, S. S. Sun, C. Guo, Z. W. Li, K. Sun, Y. Liu, W. J. Lu, Y. P. Sun, H. F. Tian, H. X. Yang, and J. Q. Li, Struct. Dyn. **4**, 044012 (2017).

[26] V. A. Lobastov, R. Srinivasan, and A. H. Zewail, Proc. Natl. Acad. Sci. USA **102**, 7069 (2005).

[27] A. H. Zewail, Science **328**, 187 (2010).

[28] D. J. Flannigan and A. H. Zewail, Acc. Chem. Res. **45**, 1828 (2012).

[29] L. Piazza, D. J. Masiel, T. LaGrange, B. W. Reed, B. Barwick, and F. Carbone, Chem. Phys. **423**, 79 (2013).

[30] D. A. Plemmons, P. K. Suri, and D. J. Flannigan, Chem. Mater. **27**, 3178 (2015).

[31] A. Adhikari, J. K. Eliason, J. Sun, R. Bose, D. J. Flannigan, and O. F. Mohammed, ACS Appl. Mater. Interfaces **9**, 3 (2017).

[32] D. H. Auston, C. V. Shank, and P. Lefur, Phys. Rev. Lett. **35**, 1022 (1975).

[33] M. C. Downer and C. V. Shank, Phys. Rev. Lett. **56**, 761 (1986).

[34] D. R. Cremons, D. A. Plemmons, and D. J. Flannigan, Nat. Commun. **7**, 11230 (2016).

[35] D. T. Valley, V. E. Ferry, and D. J. Flannigan, Nano Lett. **16**, 7302 (2016).

[36] A. J. McKenna, J. K. Eliason, and D. J. Flannigan, Nano Lett. **17**, 3952 (2017).

[37] D. R. Cremons, D. A. Plemmons, and D. J. Flannigan, Struct. Dyn. **4**, 044019 (2017).

[38] D. A. Plemmons and D. J. Flannigan, Chem. Phys. Lett. **683**, 186 (2017).

[39] J. R. Dwyer, C. T. Hebeisen, R. Ernstorfer, M. Harb, V. B. Deyirmenjian, R. E. Jordan, and R. J. D. Miller, Philos. Trans. R. Soc. A **364**, 741 (2006).

[40] G. Cao, S. Sun, Z. Li, H. Tian, H. Yang, and J. Li, Sci. Rep. **5**, 8404 (2015).

[41] See Supplemental Material at http://link.aps.org/supplemental/10.1103/PhysRevMaterials.1.073801 for UEM videos of coherent acoustic-phonon dynamics, further experimental details, determination of UEM time zero, determination of the image-contrast mechanism, determination of phonon-wave-front velocities, determination of the specimen thickness, elastic-plate dispersion calculations, and control experiments.

[42] D. J. Flannigan, D. R. Cremons, and D. T. Valley, J. Mater. Res. **32**, 239 (2017).

[43] H. Song, R. H. French, and R. L. Coble, J. Am. Ceram. Soc. **72**, 990 (1989).

[44] T. Saito, T. Hirayama, T. Yamamoto, and Y. Ikuhara, J. Am. Ceram. Soc. **88**, 2277 (2005).

[45] T. Shibata, H. Irie, D. A. Tryk, and K. Hashimoto, Phys. Chem. Chem. Phys. **12**, 7911 (2010).

[46] H. Y. Hao and H. J. Maris, Phys. Rev. Lett. **84**, 5556 (2000).

[47] P. Y. Yu and M. Cardona, *Fundamentals of Semiconductors: Physics and Materials Properties* (Springer, New York, 2016).

[48] H. M. van Driel, Phys. Rev. B **19**, 5928 (1979).

[49] E. A. Stern and D. Brewe, J. Phys. Conf. Ser. **190**, 012053 (2009).

[50] N. V. Chigarev, D. Y. Paraschuk, X. Y. Pan, and V. E. Gusev, Phys. Rev. B **61**, 15837 (2000).

[51] N. V. Chigarev, D. Y. Parashchuk, Y. S. Pan, and V. E. Gusev, J. Exp. Theor. Phys. **94**, 627 (2002).

[52] B. Y.-K. Hu, C. J. Stanton, and J. W. Wilkins, Phys. Rev. B **44**, 11067 (1991).

[53] W. M. Gao, C. Glorieux, and J. Thoen, Int. J. Eng. Sci. **41**, 219 (2003).

[54] D. Clorennec, C. Prada, D. Royer, and T. W. Murray, Appl. Phys. Lett. **89**, 024101 (2006).

[55] J. Cuffe, E. Chavez, A. Shchepetov, P. O. Chapuis, E. H. El Boudouti, F. Alzina, T. Kehoe, J. Gomis-Bresco, D. Dudek,

Y. Pennec, B. Djafari-Rouhani, M. Prunnila, J. Ahopelto, and C. M. S. Torres, Nano Lett. **12**, 3569 (2012).

[56] J. K. Yu, S. Mitrovic, D. Tham, J. Varghese, and J. R. Heath, Nat. Nanotechnol. **5**, 718 (2010).

[57] K. Biswas, J. Q. He, I. D. Blum, Chun-Iwu, T. P. Hogan, D. N. Seidman, V. P. Dravid, and M. G. Kanatzidis, Nature (London) **489**, 414 (2012).

[58] N. Stenger, M. Wilhelm, and M. Wegener, Phys. Rev. Lett. **108**, 014301 (2012).

[59] M. Maldovan, Nature (London) **503**, 209 (2013).

[60] T. Dehoux, M. A. Ghanem, O. F. Zouani, M. Ducousso, N. Chigarev, C. Rossignol, N. Tsapis, M. C. Durrieu, and B. Audoin, Ultrasonics **56**, 160 (2015).